Probing the electronic structure of bistable single-layer RbI structures on Ag(111)

Benjamin W. McDowell, Jon M. Mills,[*] Austin W. Green, Motoaki Honda, and George V. Nazin[†]

Department of Chemistry and Biochemistry, Materials Science Institute, Oregon Center for Optical, Molecular, and Quantum Science, University of Oregon, 1253 University of Oregon, Eugene, Oregon 97403, USA

Strong interactions present in single-layer RbI grown on metal surfaces have been shown to result in the surprising coexistence of bistable RbI structures. However, it is not well known how these structural differences affect the electronic behavior of the RbI film. Here, we use scanning tunneling microscopy/spectroscopy (STM/STS) to probe the image potential electronic states (IPSs) of the RbI/Ag(111) system, which are known to be highly sensitive to the electronic properties of ultrathin insulating films. By comparing our experimental STS measurements to first-principles numerical simulations of the IPSs, we calculate the work function, dielectric constant, and conduction band energy for the two distinct structure types of RbI on Ag(111). In addition, our results show that local variations in the IPS behavior, evident in both a moiré pattern and grain boundary defects, can be attributed to electrostatic potentials present in the RbI structure.

I. INTRODUCTION

As materials are reduced in scale to ultrathin layers, they can exhibit unusual electronic properties that are distinct from those found in the bulk material [1–4]. One particular example is the loss of a well-defined band gap in many ultrathin dielectrics, which poses problems in the continued effort to miniaturize electronic devices where insulating materials are a fundamental component [5]. The loss of a well-defined band gap can result, in part, from interactions with metal substrates. These interactions have been shown to impact ultrathin dielectric layers through changes in structure [6–10] and electronic properties, such as spatial modulation of both the work function [11,12] and interface electronic states [13–16]. An understanding of the relationship between ultrathin dielectrics and the substrates on which they are grown necessitates direct visualization of the atomic and electronic structure, making scanning tunneling microscopy/spectroscopy (STM/STS) a leading tool for its ability to probe these features with nanoscale resolution [17].

While there are a diverse range of choices for ultrathin dielectrics, alkali halides are a common choice for their wide band gap [18,19] and well defined atomic structure [12,20–23]. Of the alkali halides, NaCl has been the most extensively studied and has been demonstrated to be influenced by substrate interactions, which lead to formation of spatially modulated electronic states at the metal-insulator interface [13,14] and a work function that varies spatially with the substrate/adlayer registry [12]. A promising alternative to NaCl with which to study the effect of substrate-adlayer interactions in ultrathin dielectrics is RbI, which has been shown

to have stronger interactions with metal substrates due to weaker alkali-halide bonds [6,15]. These stronger interactions are evidenced by structural coupling to the metal substrate on Ag(111), where RbI was shown to form unexpected structures with hexagonal symmetry (matching that of the face-centered-cubic surface), in contrast to the square symmetry expected for typical alkali halides forming rocksaltlike structures [6]. However, it is not well understood how the strong substrate-adlayer interactions present for ultrathin RbI layers affect the electronic properties of the dielectric. It is important to understand the role of substrate-adlayer interactions in determining electronic properties of ultrathin dielectrics, as these effects have direct implications in the behavior of nanoscale electronic devices. In considering this, it is informative to consider how substrate-adlayer interactions might vary locally, for example at structural defects like those previously shown to impact local electronic structure in alkali-halide thin films [13,24–26]. Here, we use RbI to study, with STM/STS, how interactions with the substrate affect the electronic properties of ultrathin RbI on Ag(111).

II. EXPERIMENTAL AND COMPUTATIONAL METHODS

A. Experiment

Experiments were carried out in a home-built ultrahigh vacuum (UHV) cryogenic STM system, in which the bias voltage (V_b) is applied to the sample [27]. All imaging and spectroscopic measurements were carried out at 26 K using electrochemically etched silver tips [28] at a base pressure of approximately 3.0×10^{-11} torr. A Ag(111) single crystal was prepared *in situ* by sputtering with Ne followed by annealing, which was repeated for multiple cycles. A submonolayer of RbI (obtained from Sigma-Aldrich, 99.9% purity) was deposited onto the Ag surface (held at room temperature) via *in situ* sublimation under UHV conditions. After deposition

165432-1

of RbI, the sample was annealed for 1 h at approximately 320 K. All STS spectra were recorded with the feedback left on during STS acquisition, in line with previous studies of image potential electronic states (IPSs) [29].

B. Computational

Computations were performed using density functional theory (DFT) [30] as implemented by the Vienna Ab Initio Simulation Package (VASP) [31–33] with a projector-augmented plane wave basis set [34]. The Ag(111) surface was constructed with data obtained from the Materials Project [35] with approximately 25 Å of vacuum added to prevent interaction of periodic unit cells perpendicular to the surface. The hexagonal RbI structure was optimized on three layers of Ag (with the bottom layer frozen to retain the bulk lattice constant) via the PBE functional for solids (PBE$_{sol}$) [36] until all forces were less than 0.005 eV Å^{-1}, using a $5\times5\times1$ k-point mesh centered at the Γ point and a 500-eV plane-wave cutoff. The unit cell size of the square RbI structure (300 Rb, I atoms + 558 Ag atoms per layer) was prohibitive to performing calculations at the same level of accuracy, and was optimized on a single, frozen layer of Ag via the PBE$_{sol}$ functional at the Γ point with a 500-eV plane-wave cutoff until all forces were less than 0.05 eV Å^{-1}. All electronic structure calculations were optimized until the change in energy between iterative steps was less than 10^{-8} eV. To characterize charge transfer between atoms, we used Bader analysis [37–40] with a vacuum cutoff of 10^{-3} electrons Å^{-3}, which kept all atomic volumes within 5% of the average for each atomic species. The change in potential due to RbI-Ag interaction was calculated by subtracting the total potential (composed of ionic and Hartree components) of the isolated RbI/Ag structures from the composite system: $\Delta E(r) = E(r)_{Ag/RbI} - E(r)_{Ag} - E(r)_{RbI}$. Visualizations of all structures were made using the VESTA package [41].

Simulations of IPSs were performed using a Numerov-Cooley algorithm for integrating wave functions in a one-dimensional potential described elsewhere [29], where we used a spherical-tip approximation to calculate the electric field between the tip and sample [42]. The lattice component of the potential was determined by the nearly free electron model which reproduced the Ag(111) band gap [43] with values of $V_g = 2.1$ V, $V_0 = 4.634$, and a lattice spacing of 237.0 pm [35]. The thickness of the RbI monolayer was determined from experimental STM data recorded at the bias voltage of the STS set point: $w_{square} = 0.24$ nm, $w_{hexagonal} = 0.25$ nm.

III. RESULTS AND DISCUSSION

After depositing submonolayer RbI on Ag(111), we observe the coexistence of two distinct RbI structures [Fig. 1(a)], in line with previous results [6]. The structural distinctions between these RbI phases have been reported elsewhere [6], and we describe them briefly here. One RbI structure exhibits squarelike symmetry (square in the following) and is analogous to the (100) plane of bulk RbI. The other RbI structure has hexagonal-like symmetry (hexagonal in the following), adopting the symmetry of the Ag(111) surface. To explore
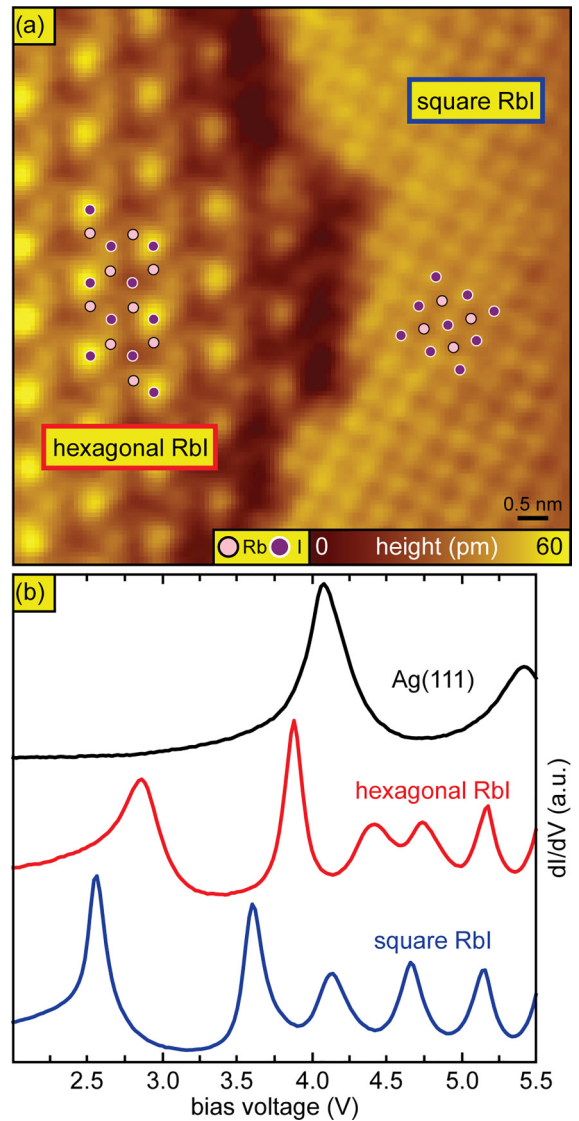

FIG. 1. Representative STS of IPS on RbI/Ag(111). (a) STM topography ($V_b = -50$ mV, $I = -200$ pA) of a region of RbI showing coexistence of hexagonal (left side) and square (right side) RbI structures. (b) Representative STS spectra ($I = 10$ pA, $V_{pp} = 40$ mV) recorded on each RbI structure type, where the feedback was left on during STS acquisition, in line with previous studies of IPS [29].

the electronic structure of each RbI structure we record STS measurements on each RbI phase, focusing on the energy range in which we expect to find image potential states (IPSs), which have been useful previously in characterizing the electronic properties of insulating thin films [12,29]. Our STS spectra show that the energies of IPSs are distinct between hexagonal and square RbI, both of which are significantly different from the spectra recorded on bare Ag(111) [Fig. 1(b)]. Importantly, the distinct IPS spectra for each RbI phase suggests a difference in electronic properties.

To understand how differences in electronic properties could result in distinct IPS spectra for each RbI structure, we have modeled our STS results using methods previously employed to simulate IPS spectra of alkali halides [29]. Here, we use a one-dimensional potential to simulate the
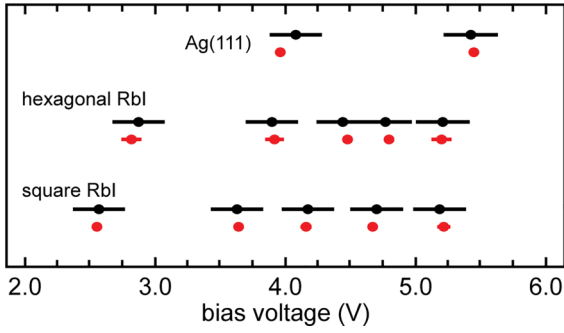
FIG. 2. Experimental and simulated IPS energies. Comparison of simulated (red) to experimental (black) IPS energies. The horizontal bars are the standard error of experimental STS data obtained with five different tips summed in quadrature with the measurement's uncertainty resulting from the amplitude of bias oscillation in the STS measurement (40 mV peak to peak).

IPS of bare Ag(111) (see Supplemental Material Fig. S1 for representative simulated wave functions [44]), which, by fitting to our experimental results [Fig. 1(b)], allows us to calculate the work function of the tip (ϕ_{tip}), the tip radius (R), and the tip-sample separation (z_0) at the low-voltage boundary of the spectra shown in Fig. 1(b) (the tip-sample separation increases in these spectra with voltage while the tunneling current is maintained constant). The values calculated for bare Ag(111) serve as input parameters for the simulation of IPS spectra on RbI, which we optimize to fit our experimental results by varying the work function of the sample (ϕ_{sample}), the dielectric constant of single-layer RbI (ε), and the conduction band energy of RbI (V_{cbm}). Our simulated IPS energies agree well with our experimental results, with all simulated energies falling within one standard error of experiment (Fig. 2), and the calculated parameters showing consistency between data sets obtained with different STM tips (Table I).

Examination of the simulated parameters in Table I shows clear distinctions in electronic properties between the two RbI structure types. Of the three parameters simulated for RbI, there are significant differences in ϕ_{sample} and ε between the two RbI structure types, while V_{cbm} shows similar values for each. Our results show that ϕ_{sample} is smaller (by 0.69 eV) on

hexagonal RbI than on square RbI, and both numbers show a reduction in work function from literature values for bare Ag(111) (4.59 eV) [45,46], in agreement with previous results for NaCl, which also showed reduced values for ϕ_{sample} [29]. The difference in ϕ_{sample} between square and hexagonal RbI is consistent with previous DFT calculations, which showed that hexagonal RbI transfers more electrons to the surface, resulting in a more significant reduction of ϕ_{sample} [6]. There is also a significant difference between the dielectric constants of hexagonal and square RbI, with the value for square RbI being greater by 1.00. Each of these values shows a significant decrease in dielectric constant relative to the bulk value (4.83) [47], which is in line with previous results for ultrathin NaCl layers [29]. The observed difference in dielectric constant between hexagonal and square RbI can be explained by the bonding at the metal/dielectric interface: iodine atoms in hexagonal RbI interact more strongly with Ag(111) than in the square RbI structure, resulting in formation of Ag-I covalent bonds near the Fermi level [6], in line with similar results for NaCl [12,22,23]. Consequently, the more significant presence of interfacial covalent bonding in the hexagonal RbI structure leads to a greater polarizability than for the square RbI structure. Finally, our simulated results show similar values for the conduction band energies of square and hexagonal RbI. This is in agreement with our DFT calculations, which show that this value is affected by conflicting factors: the reduced (increased) adlayer coordination and longer (shorter) average Rb-I bond length of hexagonal (square) RbI suggests a smaller (wider) band gap (see Supplemental Material Fig. S2 [44]), but the stronger (weaker) interaction of hexagonal (square) RbI with Ag suggests a more (less) significant widening of the band gap due to substrate-adlayer interaction (see Supplemental Material Fig. S3 [44]). Overall, we find that our calculation of electronic properties from the IPS spectra of RbI is in agreement with our DFT calculations and previous work [6].

Thus far, we have discussed the average behavior of the square and hexagonal RbI structures. However, we also observe local deviations from the described average behavior for both types of structures, both across the pristine square structure and at defects in the hexagonal structure. For the square RbI structure, we observe spatial variations in the IPS spectra that match the periodicity of the moiré structure formed between square RbI and Ag(111). This moiré pattern is characterized in detail elsewhere [6], and we briefly describe it here: the square RbI structure is incommensurate with the hexagonal symmetry of the Ag(111) surface, resulting in a moiré supercell defined by lattice vectors with magnitudes of 2.7 and 15.8 nm, which are oriented along the [11$\bar{2}$] and [1$\bar{1}$0] directions of the Ag(111) surface [Fig. 3(a)]. By recording a progression of STS spectra along the long axis of the moiré supercell, we observe that the energy of the first IPS varies with position [Fig. 3(b)], while the energy of all other IPSs remains constant. (We note that there is no spatially dependent changes in IPS energy along the short moiré axis; see Supplemental Material Fig. S4 [44].) The spatial modulation of the first IPS energy is periodic with the long axis of the moiré supercell, and it is downshifted by 0.06 V in the regions which appear taller in STM topography [dashed curve in Figs. 3(e) and 3(f)] relative to the regions which appear darker and

TABLE I. Optimized parameters used to simulate IPS spectra. The initial tip-sample separation (z_0), work function of the tip (ϕ_{tip}), and tip radius (R) were calculated by fitting simulated results to experimental STS measurements obtained with five different tips. Using the optimized parameters for each tip, results were then simulated for each RbI structure type, where the optimized parameters were the work function of the sample (ϕ_{sample}), the dielectric constant of the RbI structure (ε), and the conduction band energy (V_{cbm}). The reported values are the average and standard deviation of results using experimental STS data from five different tips.

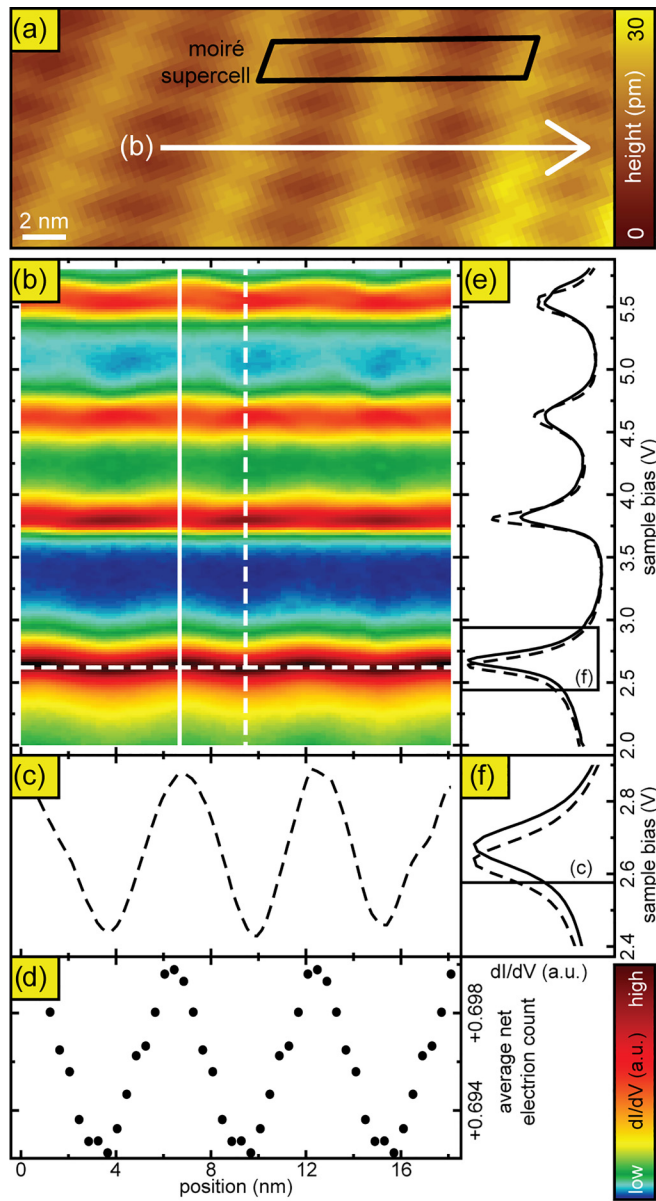|	Ag			Hexagonal RbI	Square RbI
z_0 (nm)	1.55 ± 0.09	ϕ_{sample} (eV)		2.42 ± 0.14	3.11 ± 0.07
ϕ_{tip} (eV)	3.70 ± 0.04	ε		2.98 ± 0.01	1.98 ± 0.10
R (nm)	4.33 ± 0.03	V_{cbm} (eV)		2.94 ± 0.01	3.04 ± 0.01

FIG. 3. STS measurements of spatial modulation of IPS energy in square RbI. (a) STM topography ($V_b = 2$ V, $I = 10$ pA) of a square RbI monolayer, indicating the path along which a progression of STS measurements were taken in (b). (b) Progression of STS measurements taken along the spatial path shown in (a). (c) Spatial variation in downshifted first IPS, showing STS data from the horizontal dashed line in (b). (d) Spatial variation in DFT-calculated net electron counts, averaged along the ⟨100⟩ RbI direction orthogonal to the STS path. (e) Individual STS spectra showing distinctions in energy of the lowest-energy IPS for different regions of the moiré supercell. The spectra correspond to the position of the vertical lines in (b). (f) Portion of the STS spectra from (e), zoomed in to highlight difference in the first IPS energy.

striped [solid curve in Figs. 3(e) and 3(f)]. We find that these distinct IPS energies arise from the moiré structure and can be explained by electrostatics, as detailed in the following. The spatial variations in the downshifted IPSs [Fig. 3(c)] align with DFT-calculated spatial variations in the net electron counts of iodine atoms [Fig. 3(d)], which have previously

been shown to participate more significantly than Rb atoms in transferring charge to Ag [6]. Thus, in regions where iodine transfers more electrons to the substrate, the adlayer has a more positive charge, resulting in a stabilizing effect on the IPS. Since the stabilizing electrostatic environment is localized to the adlayer, it follows that the downshifting of the IPS is only clearly observable for the first IPS, since higher order IPS states are further delocalized from the surface. We note that the observed spatial variation in the first IPS is also in agreement with previous studies of interface electronic states in the RbI/Ag(111) system, which were spatially modulated by an electrostatic potential commensurate with the moiré supercell [15].

In addition to local variations in the IPS spectra for the pristine square RbI structure, we also observe local variations at one-dimensional grain boundary defects (GBDs) in the hexagonal RbI structure [Fig. 4(a)]. To understand how these defects impact the electronic properties of hexagonal RbI, we have recorded STS spectra on many different GBDs, with representative curves shown in Fig. 4(b). A consistent result of these STS measurements is that the first IPS is downshifted at the defect relative to the pristine hexagonal structure [Fig. 4(b)]. Further, by mapping individual STS data for specific energies in two dimensions, we are able to characterize the spatial variations in the energy of the first IPS. At a bias voltage of 2.9 V, we observe high LDOS along the GBD [Fig. 4(c)], while at higher bias voltages of 3.1 V we observe high LDOS in the pristine RbI region away from the GBD [Fig. 4(d)], suggesting that the downshifted IPS is relatively delocalized along the entirety of the GBD. This finding is in agreement with previous results for RbI on Au(111) [24] and for NaCl on Ir(111) [48], which found that the LDOS was, in general, downshifted at GBDs.

To understand why the first IPS is downshifted at GBDs in the hexagonal RbI structure, we turn to DFT and, in doing so, must first characterize the atomic structure of the GBD. While our STM images do not resolve the atomic structure of the GBD, we are able to identify the discontinuity between the two pristine RbI domains, which is one Ag lattice spacing [see Fig. 5(a)] for the GBD shown in Fig. 4. Our DFT calculations indicate that it is energetically unfavorable to leave the polar edges of each RbI domain uncompensated, suggesting that the GBD region is not bare Ag(111). Instead, the two adjacent RbI domains can be bridged by the addition of individual RbI molecules, which our DFT calculations show is best accomplished by a specific atomic structure [shown in Fig. 5(a)], in line with previous structural results for GBDs in RbI on Au(111) [24] and NaCl on Ir(111) [48].

In order to understand how the GBD might affect the IPSs locally, it is instructive to visualize the DFT-calculated change in potential energy of electrons due to adsorption of RbI, as shown in Fig. 5(b). From this we observe that, in general, iodine (Rb) atoms induce a local decrease (increase) in potential energy, which is a result of the metal surface screening the polar adlayer atoms. Screening of the adlayer atoms by the Ag surface leads to electron depletion (accumulation) near the negatively (positively) charged iodine (Rb) atoms, resulting in local decreases (increases) in potential energy. However, the effect of adsorption on the potential energy is not consistent for each adlayer atom, as is most
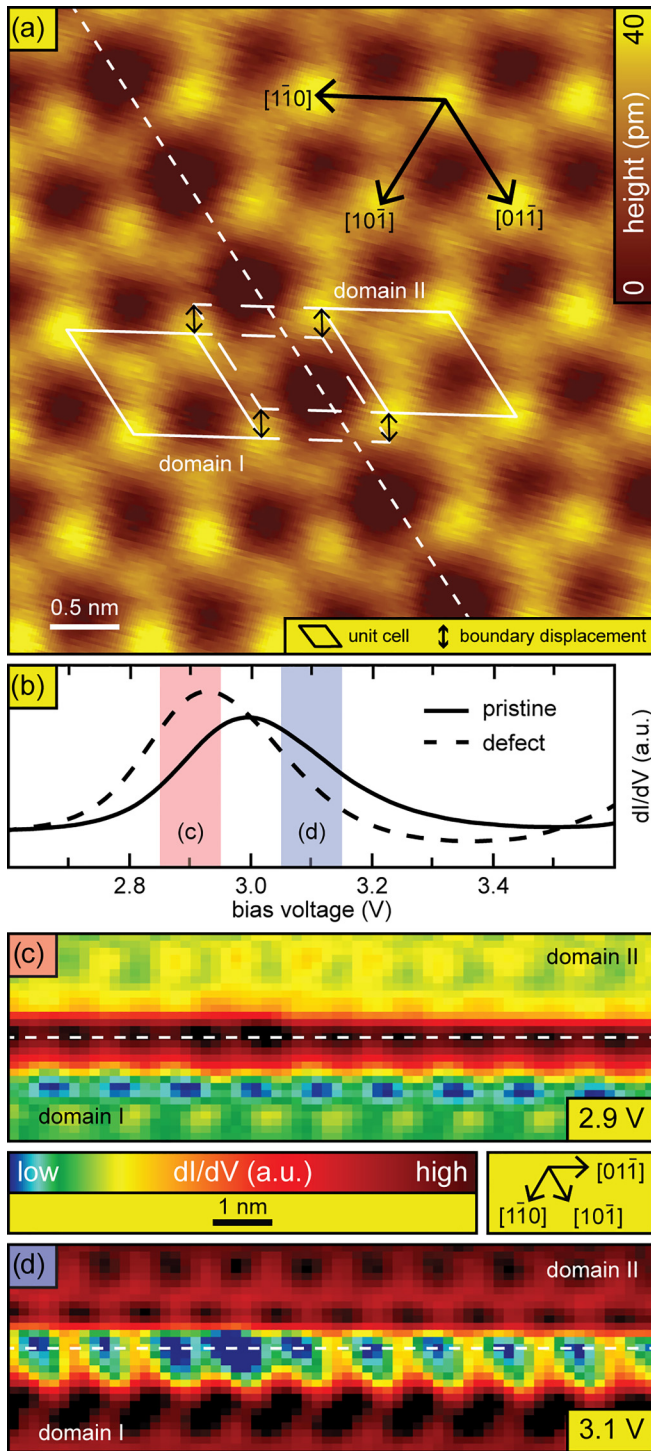
FIG. 4. STS results for localized IPS at GBD in hexagonal RbI. (a) STM topography ($V_b = 50$ mV, $I = 10$ pA) of GBD formed between two discontinuous domains of hexagonal RbI, where the pristine unit cell is shown in white and the discontinuity is highlighted by the double-sided arrows. (b) Representative STS measurements taken on (dashed curve) and away from (solid curve) the GBD shown in (a). The energy ranges used for two-dimensional STS mapping are overlaid in red (c) and blue (d). (c), (d) Two-dimensional STS mapping of the GBD shown in (a), where the mapped energies are chosen to show the spatial behavior of the downshifted IPS at the GBD (c) and the IPS of the pristine hexagonal monolayer (d). The horizontal dashed line shows the orientation of the GBD as in (a).

clearly evidenced by iodine atoms, which have previously been shown to be more sensitive to adsorption site placement than Rb atoms [6]. The effect of distinct adsorption sites can be seen by comparing the change in potential energy for the three distinct adsorption sites in the pristine hexagonal RbI structure: iodine atoms coordinated to a single Ag atom (I_{top}) have a less stabilizing effect than those coordinated to three Ag atoms ($I_{hcp-hollow}$ and $I_{fcc-hollow}$) [Fig. 5(c)]. Our DFT results suggest that this difference in electrostatic behavior between distinct adsorption sites is the result of differences in I-Ag charge transfer, where iodine atoms coordinated to three Ag atoms have lower net electron counts ($+0.60$ electrons) than those coordinated to a single Ag atom ($+0.67$ electrons) on average, in agreement with previous studies of hexagonal RbI on Ag(111) which showed that higher coordination of iodine to Ag leads to increased electron transfer to the substrate [6]. The distinct changes in potential for each adsorption site are thus a result of electrostatics, where the less (more) negatively charged iodine atoms yield a more (less) stabilizing potential.

Importantly, our results show that the effect of reduced coordination within the adlayer is consequential at the GBD, where the electrostatic environment is more stabilizing than in the pristine RbI structure [compare I_{defect} to $I_{hcp/fcc-hollow}$ in Fig. 5(c)]. At the GBD, there is significantly less coordination within the adlayer, as highlighted by a longer than average Rb-I bond length (4.50 Å at the defect vs 3.97 ± 0.12Å in the pristine hexagonal structure). This distinction in adsorption site is accompanied by a significant increase in I-Ag electron transfer, resulting in a smaller net electron count for iodine atoms at the GBD ($+0.50$ electrons) relative to those in the pristine hexagonal RbI structure ($+0.62$ electrons, on average). In contrast, despite a similarly increased Rb-I bond length, Rb atoms at the defect show similar net electron counts when compared to the pristine hexagonal RbI structure (-0.83 vs -0.84 electrons), in agreement with previous studies of RbI on Ag(111), which found that Rb atoms are less sensitive to adsorption site placement than iodine atoms. Thus, the smaller net electron counts for iodine atoms at the GBD lead to a stabilizing potential, which lowers the energy of the first IPS. This effect is only observed for the first IPS, since higher-order IPS are less confined to the surface and less sensitive to changes in the potential at the adlayer. Furthermore, while we have presented data on only a single GBD structure here, our STS results show that other RbI GBDs behave similarly on Ag(111), which our interpretation suggests is due to local stabilizing electrostatic potentials arising from increased substrate-adlayer interaction at the defect. The physical picture offered here may be similar for GBDs in other ultrathin dielectrics where substrate adlayer interactions are locally stronger at the defect.

IV. CONCLUSION

To summarize, we have used STM/STS to study image potential states associated with two structurally different phases of single-layer RbI on Ag(111). By comparing experimental STS data to simulations, we have quantitatively evaluated the electronic properties of these two RbI structures, revealing notable disparities in the electrostatic behavior of the two
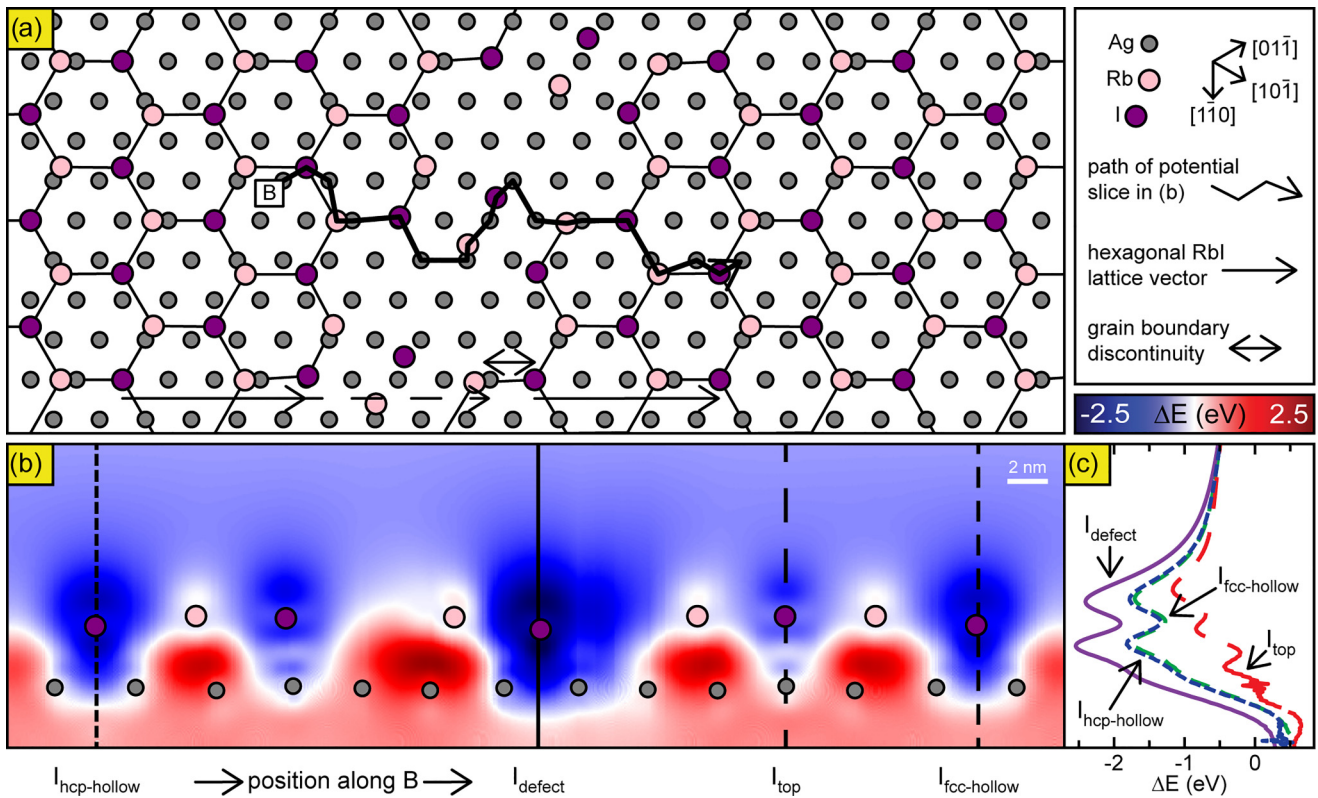
FIG. 5. DFT-calculated potential for GBD in hexagonal RbI. (a) DFT-optimized structure of the GBD shown in Fig. 4. The solid horizontal arrows show the lattice vector of the pristine hexagonal RbI structure, the dashed arrow shows how the pristine lattice vector propagates across the GBD, and the double-sided arrow shows the discontinuity between the structures on either side of the GBD. The segmented solid arrow shows the path along which the change in potential is sliced in (b). (b) Change in potential energy of electrons due to adsorption of RbI $[\Delta E(r) = E(r)_{Ag/RbI} - E(r)_{Ag} - E(r)_{RbI}]$, is shown in the direction orthogonal to the surface. (c) Vertical slices of the potential from (b) are shown for several iodine atoms with distinct adsorption geometry, as indicated by the vertical lines shown in (b).

distinct structural phases. In line with these results, we find that variations in the local electrostatic environment are, to a large extent, responsible for local variations in the image potential state behavior, arising from the moiré pattern of the square RbI structure and defects in the hexagonal RbI structure. The comparison of electrostatic behavior between the two RbI structure types and characterization of local variations in each structure type offers insight on how substrate-adlayer interactions can impact the adlayer electronic properties.

[1] C. Tan, X. Cao, X. Wu, Q. He, J. Yang, X. Zhang, J. Chen, W. Zhao, S. Han, G. Nam *et al.*, Recent advances in ultrathin two-dimensional nanomaterials, Chem. Rev. **117**, 6225 (2017).

[2] Y. Liu, X. Duan, Y. Huang, and X. Duan, Two-dimensional transistors beyond graphene and TMDCs, Chem. Soc. Rev. **47**, 6388 (2018).

[3] G. S. Parkinson, Iron oxide surfaces, Surf. Sci. Rep. **71**, 272 (2016).

[4] L. Gao, X. Cui, C. D. Sewell, J. Li, and Z. Lin, Recent advances in activating surface reconstruction for the high-efficiency oxygen evolution reaction, Chem. Soc. Rev. **50**, 8428 (2021).

[5] Y. Y. Illarionov, T. Knobloch, M. Jech, M. Lanza, D. Akinwande, M. I. Vexler, T. Mueller, M. C. Lemme, G. Fiori,

F. Schwierz *et al.*, Insulators for 2D nanoelectronics: The gap to bridge, Nat. Commun. **11**, 3385 (2020).

[6] B. W. McDowell, J. M. Mills, M. Honda, and G. V. Nazin, Structural bistability in RbI monolayers on Ag(111), J. Phys. Chem. Lett. **14**, 3023 (2023).

[7] S. Matencio, E. Barrena, and C. Ocal, Coming across a novel copper oxide 2D framework during the oxidation of Cu(111), Phys. Chem. Chem. Phys. **18**, 33303 (2016).

[8] C. Möller, J. Barreto, F. Stavale, and N. Nilius, Manganese oxide thin films on Au(111): Growth competition between MnO and Mn_3O_4, J. Phys. Chem. C **123**, 7665 (2019).

[9] X. Shao, N. Nilius, P. Myrach, H.-J. Freund, U. Martinez, S. Prada, L. Giordano, and G. Pacchioni, Strain-induced formation

of ultrathin mixed-oxide films, Phys. Rev. B **83**, 245407 (2011).

[10] J. Schoiswohl, M. Sock, S. Eck, S. Surnev, M. G. Ramsey, F. P. Netzer, and G. Kresse, Atomic-level growth study of vanadium oxide nanostructures on Rh(111), Phys. Rev. B **69**, 155403 (2004).

[11] H. M. Benia, P. Myrach, N. Nilius, and H. J. Freund, Structural and electronic characterization of the MgO/Mo(0 0 1) interface using STM, Surf. Sci. **604**, 435 (2010).

[12] M. Pivetta, F. Patthey, M. Stengel, A. Baldereschi, and W. D. Schneider, Local work function Moiré pattern on ultrathin ionic films: NaCl on Ag(100), Phys. Rev. B **72**, 115404 (2005).

[13] K. Kolpatzeck, L. Brendel, R. Möller, R. Robles, and N. Lorente, Paradoxical effects for a one-dimensional periodic potential embedded in a two-dimensional system, Phys. Rev. B **107**, 155418 (2023).

[14] J. Repp, G. Meyer, and K. H. Rieder, Snell's law for surface electrons: Refraction of an electron gas imaged in real space, Phys. Rev. Lett. **92**, 036803 (2004).

[15] B. W. McDowell, J. M. Mills, M. Honda, and G. V. Nazin, Spatially modulated interface states in a two-dimensional potential: Single-layer RbI on Ag(111), J. Chem. Phys. **159**, 224705 (2023).

[16] Y. Pan, S. Benedetti, N. Nilius, and H. J. Freund, Change of the surface electronic structure of Au(111) by a monolayer MgO(001) film, Phys. Rev. B **84**, 075456 (2011).

[17] K. Bian, C. Gerber, A. J. Heinrich, D. J. Müller, S. Scheuring, and Y. Jiang, Scanning probe microscopy, Nat. Rev. Methods Primers **1**, 1 (2021).

[18] D. Fröhlich and B. Staginnus, New assignment of the band gap in the alkali bromides by two-photon spectroscopy, Phys. Rev. Lett. **19**, 496 (1967).

[19] F. C. Brown, C. Gähwiller, H. Fujita, A. B. Kunz, W. Scheifley, and N. Carrera, Extreme-ultraviolet spectra of ionic crystals, Phys. Rev. B **2**, 2126 (1970).

[20] W. Hebenstreit, J. Redinger, Z. Horozova, M. Schmid, R. Podloucky, and P. Varga, Atomic resolution by STM on ultrathin films of alkali halides: Experiment and local density calculations, Surf. Sci. **424**, L321 (1999).

[21] X. Sun, M. P. Felicissimo, P. Rudolf, and F. Silly, NaCl multi-layer islands grown on Au(111)-() probed by scanning tunneling microscopy, Nanotechnology **19**, 495307 (2008).

[22] F. E. Olsson and M. Persson, A density functional study of adsorption of sodium-chloride overlayers on a stepped and a flat copper surface, Surf. Sci. **540**, 172 (2003).

[23] F. E. Olsson, M. Persson, J. Repp, and G. Meyer, Scanning tunneling microscopy and spectroscopy of NaCl overlayers on the stepped Cu(311) surface: Experimental and theoretical study, Phys. Rev. B **71**, 075419 (2005).

[24] B. W. McDowell, B. N. Taber, J. M. Mills, C. F. Gervasi, M. Honda, and G. V. Nazin, Modulation of carbon nanotube electronic structure by grain boundary defects in RbI on Au(111), J. Phys. Chem. Lett. **15**, 439 (2024).

[25] S. Heidorn, C. Bertram, J. Koch, K. Boom, F. Matthaei, A. Safiei, J. Henzl, and K. Morgenstern, Influence of substrate surface-induced defects on the interface state between NaCl(100) and Ag(111), J. Phys. Chem. C **117**, 16095 (2013).

[26] J. Repp, G. Meyer, S. Paavilainen, F. E. Olsson, and M. Persson, Scanning tunneling spectroscopy of Cl vacancies in NaCl films: Strong electron-phonon coupling in double-barrier tunneling junctions, Phys. Rev. Lett. **95**, 225503 (2005).

[27] J. D. Hackley, D. A. Kislitsyn, D. K. Beaman, S. Ulrich, and G. V. Nazin, High-stability cryogenic scanning tunneling microscope based on a closed-cycle cryostat, Rev. Sci. Instrum. **85**, 103704 (2014).

[28] B. N. Taber, M. L. Neill, T. N. Thom, O. D. Clapp, and J. Lee, In situ plasmonic tip preparation and validation techniques for scanning tunneling microscopy, J. Vac. Sci. Technol. A **41**, 053205 (2023).

[29] H. C. Ploigt, C. Brun, M. Pivetta, F. Patthey, and W. D. Schneider, Local work function changes determined by field emission resonances: NaCl/Ag(100), Phys. Rev. B **76**, 195404 (2007).

[30] W. Kohn and L. J. Sham, Self-consistent equations including exchange and correlation effects, Phys. Rev. **140**, A1133 (1965).

[31] G. Kresse and J. Furthmüller, Efficiency of ab-initio total energy calculations for metals and semiconductors using a plane-wave basis set, Comput. Mater. Sci. **6**, 15 (1996).

[32] G. Kresse and J. Furthmüller, Efficient iterative schemes for ab initio total-energy calculations using a plane-wave basis set, Phys. Rev. B **54**, 11169 (1996).

[33] G. Kresse and J. Hafner, Ab initio molecular dynamics for liquid metals, Phys. Rev. B **47**, 558 (1993).

[34] P. E. Blöchl, Projector augmented-wave method, Phys. Rev. B **50**, 17953 (1994).

[35] R. Tran, Z. Xu, B. Radhakrishnan, D. Winston, W. Sun, K. A. Persson, and S. P. Ong, Surface energies of elemental crystals, Sci. Data **3**, 160080 (2016).

[36] J. P. Perdew, A. Ruzsinszky, G. I. Csonka, O. A. Vydrov, G. E. Scuseria, L. A. Constantin, X. Zhou, and K. Burke, Restoring the density-gradient expansion for exchange in solids and surfaces, Phys. Rev. Lett. **100**, 136406 (2008).

[37] G. Henkelman, A. Arnaldsson, and H. Jónsson, A fast and robust algorithm for Bader decomposition of charge density, Comput. Mater. Sci. **36**, 354 (2006).

[38] E. Sanville, S. D. Kenny, R. Smith, and G. Henkelman, Improved grid-based algorithm for Bader charge allocation, J. Comput. Chem. **28**, 899 (2007).

[39] W. Tang, E. Sanville, and G. Henkelman, A grid-based Bader analysis algorithm without lattice bias, J. Phys.: Condens. Matter **21**, 084204 (2009).

[40] M. Yu and D. R. Trinkle, Accurate and efficient algorithm for Bader charge integration, J. Chem. Phys. **134**, 64111 (2011).

[41] K. Momma and F. Izumi, VESTA 3 for three-dimensional visualization of crystal, volumetric and morphology data, J. Appl. Crystallogr. **44**, 1272 (2011).

[42] P. Morse and H. Feshbach, *Methods of Theoretical Physics* (McGraw-Hill, York, PA, 1953), Vol. 2.

[43] N. V. Smith, C. T. Chen, and M. Weinert, Distance of the image plane from metal surfaces, Phys. Rev. B **40**, 7565 (1989).

[44] See Supplemental Material at http://link.aps.org/supplemental/10.1103/PhysRevB.109.165432 for depictions of the wave functions and potential used in the numerical simulation of IPSs, DFT-calculated LDOS of single-layer RbI structures, and STS measurements of spatial variations in the energy of IPSs along the short moiré axis. The Supplemental Material also contains Ref. [29].

[45] P. J. Blowey, B. Sohail, L. A. Rochford, T. Lafosse, D. A. Duncan, P. T. P. Ryan, D. A. Warr, T. Lee, G. Costantini, R. J. Maurer Alkali doping leads to charge-transfer salt formation in a two-dimensional metal–organic framework, ACS Nano **14**, 7475 (2020).

[46] A. Haags, L. A. Rochford, J. Felter, P. J. Blowey, D. A. Duncan, D. P. Woodruff, and C. Kumpf, Growth and evolution of tetracyanoquinodimethane and potassium coadsorption phases on Ag(111), New J. Phys. **22**, 063028 (2020).

[47] K. Kamiyoshi and Y. Nigara, Dielectric constant of some alkali halides, Phys. Status Solidi **3**, 735 (1970).

[48] X. Tan, J. Pan, J. Feng, Z. Zhang, M. Liu, D. Ma, and X. Qiu, One-dimensional periodic buckling at a symmetry-incompatible heterointerface of the NaCl(001) monolayer on Ir(111), J. Phys. Chem. C **127**, 6109 (2023).